AGU PUBLICATIONS

JGR

Journal of Geophysical Research: Oceans

RESEARCH ARTICLE

10.1002/2017JC013073

Key Points:
- Meridional variation of air-sea interactions and MLT budget in the BoB in response to MISO using RAMA moorings observation
- Mixed layer heating during active phase of MISO due to net heat into the Ocean
- ML cools during active phase of MISO in response net heat loss from the ocean to the atmosphere plus entrainment cooling at the base of ML

Supporting Information:
- Supporting Information S1

Correspondence to:
M. S. Girishkumar,
girish@incois.gov.in

Citation:
Girishkumar, M. S., Joseph, J., Thangaprakash, V. P., Pottapinjara, V., & McPhaden, M. J. (2017). Mixed layer temperature budget for the northward propagating Summer Monsoon Intraseasonal Oscillation (MISO) in the Central Bay of Bengal. *Journal of Geophysical Research: Oceans*, *122*, 8841–8854. https://doi.org/10.1002/2017JC013073

Received 8 MAY 2017
Accepted 28 SEP 2017
Accepted article online 6 OCT 2017
Published online 19 NOV 2017

Mixed Layer Temperature Budget for the Northward Propagating Summer Monsoon Intraseasonal Oscillation (MISO) in the Central Bay of Bengal

M. S. Girishkumar[1], J. Joseph[1], V. P. Thangaprakash[1], V. Pottapinjara[1], and M. J. McPhaden[2]

[1]Indian National Centre for Ocean Information Services, Hyderabad, India, [2]NOAA/Pacific Marine Environmental Laboratory, Seattle, WA, USA

Abstract Composite analyses of mixed layer temperature (MLT) budget terms from near-surface meteorological and oceanic observations in the central Bay of Bengal are utilized to evaluate the modulation of air-sea interactions and MLT processes in response to the summer monsoon intraseasonal oscillation (MISO). For this purpose, we use moored buoy data at 15°N, 12°N, and 8°N along 90°E together with TropFlux meteorological parameters and the Ocean Surface Current Analyses Real-time (OSCAR) current product. Our analysis shows a strong cooling tendency in MLT with maximum amplitude in the central and northern BoB during the northward propagation of enhanced convective activity associated with the active phase of the MISO; conversely, warming occurs during the suppressed phase of the MISO. The surface mixed layer is generally heated during convectively inactive phases of the MISO primarily due to increased net surface heat flux into the ocean. During convectively active MISO phases, the surface mixed layer is cooled by the combined influence of net surface heat loss to the atmosphere and entrainment cooling at the base of mixed layer. The variability of net surface heat flux is primarily due to modulation of latent heat flux and shortwave radiation. Shortwave is mostly controlled by an enhancement or reduction of cloudiness during the active and inactive MISO phases and latent heat flux is mostly controlled by variations in air-sea humidity difference.

1. Introduction

The northward propagation of organized convection and rainfall from the equatorial Indian Ocean to the Indian subcontinent on intraseasonal time scales of 30–60 days is one of the most prominent features during northern summer. This phenomenon is commonly known as the summer monsoon intraseasonal oscillation (MISO) (Annamalai & Slingo, 2001; Goswami, 2011; Sikka & Gadgil, 1980; Yasunari, 1979) for which rainfall anomalies extend from the eastern Arabian Sea to the western Pacific. MISOs significantly affect the seasonal mean Indian summer monsoon rainfall and thus its interannual variability (Goswami & Ajaya Mohan, 2001; Goswami et al., 2006). Hence, it is important to accurately represent the spatiotemporal evolution of MISO amplitude and frequency in coupled models for better prediction of seasonal mean and subseasonal monsoon rainfall over India and nearby land masses (Goswami & Ajaya Mohan, 2001; Goswami et al., 2006).

Recent observational and modeling efforts based on coupled and standalone atmospheric models experiments have shown that air-sea interactions are an integral part of MISO dynamics helping to determine its amplitude and northward propagation characteristics (Bhat et al., 2004; Kemball-Cook et al., 2002; Sengupta et al., 2001; Seo et al., 2007; Sharmila et al., 2013; Roxy et al., 2012; Vecchi & Harrison, 2002; Webster et al., 2002). Although extensive studies have been carried out to understand the processes associated with MISO variability, model simulations have difficulty in accurately reproducing MISO spatiotemporal evolution, particularly its northward propagation and amplitude (Lin et al., 2006). This emphasizes that to improve MISO modeling and forecasting, it is important to improve our knowledge of air-sea interaction processes that modulate mixed layer temperature (MLT) on intraseasonal time scales.

The Bay of Bengal (BoB) is one of the freshest oceanic basins in the tropics with a persistent strong halocline and thick barrier layer (the layer between the base of the salt stratified mixed layer and the top of the thermocline) due to the large amount of freshwater flux from river input and precipitation (Girishkumar et al.,

2011; Thadathil et al., 2007; Varkey et al., 1996). Earlier studies have shown that the BoB is one of the regions in the Indo-Pacific basin with high amplitude intraseasonal oscillations associated with the MISO (Fu & Wang, 2004). Hence, a better understanding about the processes that modulate the MLT balance and air-sea interaction on MISO time scales in the BoB will enhance our knowledge on the amplification and northward propagation of MISO variability and its predictability (Goswami et al., 2016).

The Madden-Julian Oscillation (MJO) is a dominant component of the tropical ISO (Madden & Julian, 1994), occurring with almost the same frequency as the MISO. The MJO impact on MLT was examined from high quality moored buoy and other observations in the equatorial Indian Ocean region in several recent studies (Chi et al., 2014; Drushka et al., 2012; McPhaden & Foltz, 2013). However, similar kinds of studies have not yet been performed on MISO time scales in the BoB. Parampil et al. (2010) examined the mixed layer heat budget on intraseasonal time scales in the BoB during the summer monsoon, but their study was based on Argo data with coarse temporal resolution (~10 days) and satellite based surface heat flux.

The availability of high quality in situ upper ocean and surface meteorological observations from Research Moored Array for African-Asian-Australian Monsoon Analysis and Prediction (RAMA) moored buoys at 8°N, 12°N, and 15°N along 90°E in the central BoB (McPhaden et al., 2009) provides a unique opportunity to quantify the MLT budget and air-sea interactions in response to northward propagating MISO variability (Figures 1 and 2). Our study uses the MISO index proposed by Suhas et al. (2013), which divides the MISO life cycle into eight phases that correspond to the shifting location of maximum intraseasonal rainfall anomalies. A detailed description of the MISO index can be found in the supporting information Text S1 and Figure S1 (Suhas et al., 2013; Wang et al., 2006; Wheeler & Hendon, 2004). Here we examine composite MLT budget terms and near-surface meteorological parameters for different phases of the MISO at RAMA mooring locations in the BoB to describe the upper ocean response to northward propagating MISO convective anomalies in the central BoB.

The paper is organized as follows. In section 2, we describe the data sets used in this study and the method used to estimate MISO signals and the MLT budget. The composite evolution of radiative and turbulent heat fluxes and MLT budget terms under different phases of the MISO are presented in section 3. The results are summarized and discussed in section 4.

2. Data and Methods

In this study, we use data available from the RAMA mooring at 8°N, 90°E for 2007–2016 and at 12°N and 15°N, 90°E for 2008–2016 during the summer monsoon season (which we define as 1 May to 30 September). RAMA buoys provide daily time series of temperature, $T(z)$ and salinity, $S(z)$, at depths z of 1, 5, 10, 20, 40, 60, 80, 100, 120, 140, 180, 300, and 500 m and 1, 5, 10, 20, 40, 60, and 100 m, respectively. We consider measurements at 1 m depth as nominally from the surface. The data are linearly interpolated in the vertical to 1 m intervals to facilitate analysis.

Mixed layer depth (MLD) is defined as the depth where the density is equal to the sea surface density plus an increment equivalent to the density change (~0.15 kg m^{-3}). This density change would be associated with change in temperature of 0.5°C in the absence of vertical salinity variations. The isothermal layer depth (ILD) is defined as the depth where the temperature is 0.5°C lower than SST. BLT is defined as the difference between ILD and MLD (Girishkumar et al., 2013).

The MLT budget is examined using the expression given by Rao and Sivakumar (2000) and Girishkumar et al. (2013):

$$\underbrace{\frac{\partial T}{\partial t}}_{(a)} = \underbrace{\frac{Q_{net}-Q_{pen}}{\rho C_p h}}_{(b)} - \underbrace{\left[u\frac{\partial T}{\partial x}+v\frac{\partial T}{\partial y}\right]}_{(c)} - \underbrace{H\left[W_h+\frac{\partial h}{\partial t}\right]\frac{(T_h-T)}{h}}_{(d)} + \underbrace{\text{Residual}}_{(e)} \quad (1)$$

The individual terms of equation (1) represent (a) temperature tendency, (b) net surface heat flux, (c) horizontal advection, (d) vertical processes (sum of entrainment and vertical advection), and (e) residual. The temperature averaged over mixed layer is designated as T, t is time, ρ is the density of seawater, C_p is specific heat capacity of seawater, h is MLD, T_h is the temperature of water entrained into the ML, taken to be temperature at 5 m below MLD (Du et al., 2005), and W_h is vertical advection below the mixed layer inferred

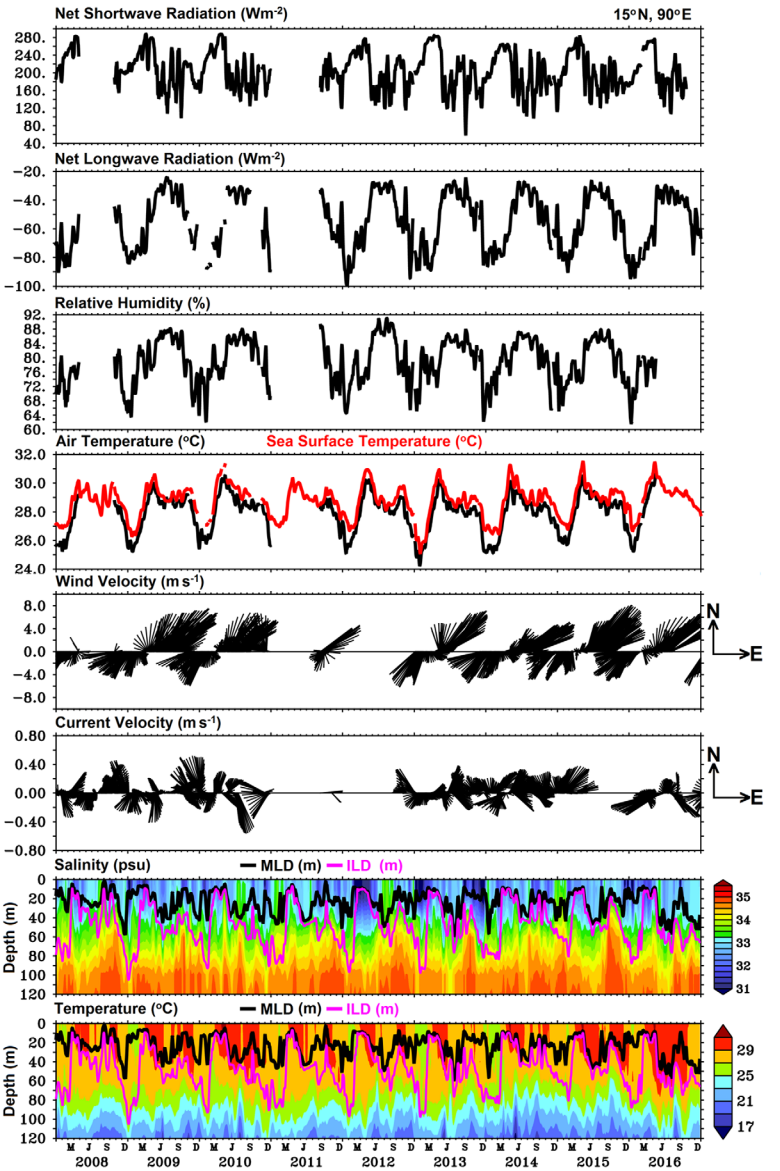

Figure 1. Temporal evolution of net shortwave radiation (W m^{-2}), net longwave radiation (W m^{-2}), relative humidity (%), air temperature (black line; °C) and SST (red line; °C), wind velocity (m s^{-1}), current velocity (m s^{-1}), salinity (psu), and temperature (°C) obtained from RAMA mooring at 15°N, 90°E in the BoB. In the bottom two plots, black and pink lines represent MLD (m) and ILD (m), respectively. All the time series variables are smoothed with a 10 day running mean.

from the vertical displacement of isotherms in the thermocline as suggested by McPhaden (1982). We have chosen the depth of 23°C isotherm as an indicator of thermocline depth in the BoB for this study, with vertical velocity (W_h, in m d^{-1}) below the mixed layer inferred from the time rate of change of the 23°C isotherm depth. The entrainment velocity (in m d^{-1}) at the base of the mixed layer is estimated from W_h and the rate of change of MLD ($\partial h/\partial t$). H is the Heaviside step function [=0 if $(W_h + \partial h/\partial t) < 0$, =1 if $(W_h + \partial h/\partial t > 0]$ (Girishkumar et al., 2013).

Latent (Q_{Latent}) and sensible ($Q_{Sensible}$) heat fluxes are estimated from the Coupled Ocean-Atmosphere Response Experiment (COARE 3.0b) bulk flux algorithm (Fairall et al., 2003) using the mooring SST, wind speed, relative humidity, and air temperature. Net surface shortwave radiation ($Q_{Shortwave}$) is obtained from downwelling shortwave flux measured from the mooring and corrected for albedo at the sea surface (downwelling short wave radiation × 0.945). Q_{Net} is the net surface heat flux term ($Q_{Shortwave} - Q_{Pen} + Q_{Longwave} + Q_{Latent} + Q_{Sensible}$). Following Morel and Antoine (1994), the penetrating short wave radiation

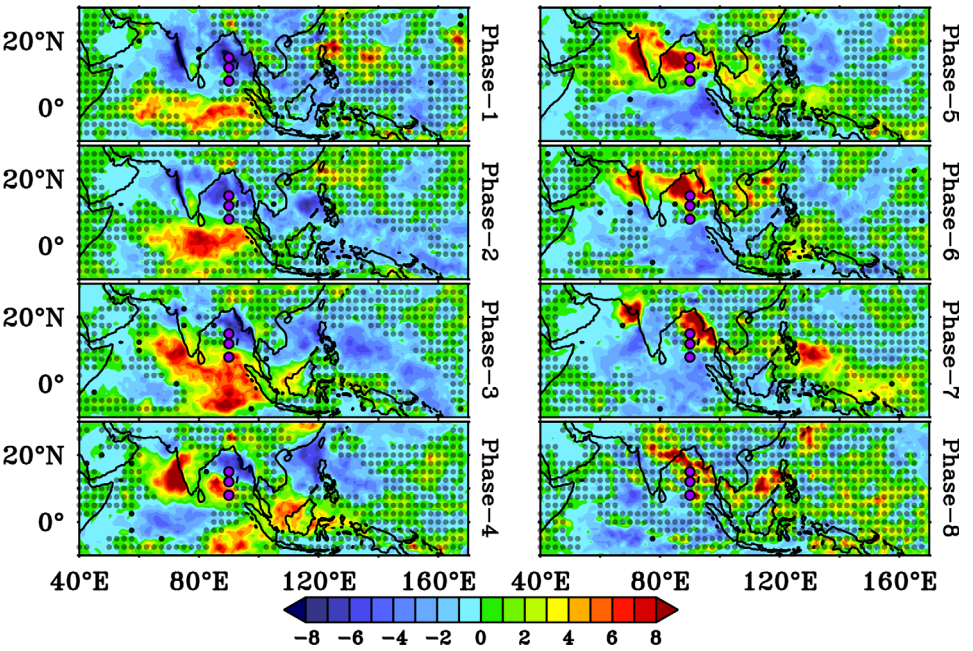

Figure 2. The composite (2007–2016) of TRMM3b42 rainfall anomaly (mm d^{-1}) under different phases of the MISO. The pink circles indicates RAMA buoy locations at 8°N, 12°N, and 15°N along 90°E. Stippling indicates values that are not significantly different from zero at the 90% confidence level using a *t* test.

(Q_{Pen}) below the mixed layer is estimated by$Q_{Pen}=0.47Q_{Shortwave}\left[V_1e^{-h/\zeta_1}+V_2e^{-h/\xi 2}\right]$, where ζ_1 and ζ_2 are the attenuation depths of long visible and short visible and ultraviolet wavelengths, and h is the MLD in meters. The values of V_1, V_2, ζ_1, and ζ_2 are estimated from MODIS monthly composite chlorophyll-*a* (mg m^{-3}) data using the method from Morel and Antoine (1994).

Optimal interpolated (OI) TRMM Microwave Imager (TMI) + Advanced Microwave Scanning Radiometer for EOS (AMSR-E) SST product (OI-SST) with 0.25° resolution (~25 km) (Gentemann et al., 2004) averaged over 50 km on either side of the buoy location were used to estimate the horizontal gradient of SST in equation (1). The zonal (*U*) and meridional (*V*) component of velocity at 10 m depth are obtained from the RAMA buoys. The residual term includes horizontal and vertical diffusive heat fluxes plus errors from a variety of sources: instrumental errors of the buoy measurements; errors in parameterizing vertical processes and surface heat fluxes from bulk formulae; computational errors associated with finite differencing; and sampling errors (Foltz et al., 2009; Vialard et al., 2008).

Though *T*(*z*) and *S*(*z*) records are very complete at all the RAMA mooring locations in the BoB, the surface meteorology and current observations have less data coverage particularly at 8°N, 90°E and 12°N, 90°E during the study period. Hence, the number of MISO events observed at these moorings with complete observations is relatively small (four MISO events) and inadequate by themselves to construct the statistical evolution of the MISO compared to 15°N, 90°E (eight MISO events). However, we can supplement with TropFlux flux data, which has been calibrated against tropical moored buoys and is a very good substitute for in situ air-sea flux for the missing buoy data (Praveen Kumar et al., 2012). Moreover, Ocean Surface Current Analysis Real-time (OSCAR) surface currents (Bonjean & Lagerloef, 2002) with 0.3° × 0.3° spatial resolution show good agreement with 10 m currents observed from the RAMA moorings in the BoB (supporting information Figures S2, S3; Table S1) though consistent with earlier studies in the Indian Ocean zonal velocity is better represented than meridional velocity in the OSCAR product (Sikhakolli et al., 2012; Sivareddy et al., 2015).

Hence, we replaced missing buoy atmospheric flux and current data, respectively, with air-sea flux data from TropFlux and zonal and meridional velocity from OSCAR to increase the number of MISO events captured at 8°N and 12°N. We then performed MLT budget calculations for two different combinations of data: RAMA *T*(*z*), RAMA *S*(*z*), RAMA Current, and RAMA Flux (defined as the RAMA analysis in the rest of paper), and RAMA *T*(*z*), RAMA *S*(*z*), OSCAR current, Tropflux flux data (defined as the RAMA+ analysis in the rest of paper).

Table 1
The Duration Individual MISO Events During the Study Period of 2007–2016

		15°N		12°N		8°N	
		RAMA	RAMA+	RAMA	RAMA+	RAMA	RAMA+
2007							
1	9 Jun:8 Jul					X	X
2	15 Jul:12 Aug					X	X
3	16 Aug:06 Sep					X	√
2008							
4	29 May:20 Jun	X	√	√	√	X	√
5	13 Jul:20 Aug	X	√	√	√	X	√
6	23 Aug:17 Sep	X	√	X	√	X	√
2009							
7	12 May:06 Jun	√	√	X	X	X	X
8	11 Jun:20 Jul	√	√	X	X	X	X
9	30 Jul: 31 Aug	√	√	X	X	X	X
2010							
10	13 May:30 May	√	√	X	√	X	X
11	3 Jun:24 Jun	√	√	X	√	X	X
12	26 Jun:14 Jul	√	√	X	√	X	X
13	14 Aug:5 Sep	X	√	X	√	X	X
2011							
14	23 May:15 Jun	X	X	X	X	√	√
15	24 Jun:15 Jul	X	X	X	X	√	√
2012							
16	18 Aug:15 Sep	X	√	X	X	√	√
17	20 Sep:30 Sep	X	√	X	√	√	√
2013							
18	25 Aug:30 Sep	X	√	X	√	X	X
2014							
19	25 Jun:22 Jul	√	√	√	√	X	X
20	20 Aug:9 Sep	√	√	√	√	X	X
2015							
21	10 May:26 May	X	√	X	√	X	√
22	27 May:29 Jun	X	√	X	√	X	√
23	11 Jul:3 Aug	X	√	X	√	X	√
2016							
24	23 May:22 Jun	X	√	X	X	X	√
25	25 Jun:23 Jul	X	√	X	X	X	√
	Total events	22	22	22	22	25	25
	Total selected events	8	20	4	15	4	13

Note. The events used for RAMA analyses (RAMA *T*(*z*), RAMA *S*(*z*), RAMA Current, RAMA Flux) and RAMA+ (RAMA *T*(*z*), RAMA *S*(*z*), OSCAR based Current, Tropflux based Flux) are marked by "√" with missing events marked by "X." The RAMA mooring site at 8°N, 90°E was first occupied in November 2006 while sites at 12°N and 15°N, 90°E were first occupied in November 2007.

Following Suhas et al. (2013), six hourly Outgoing Longwave Radiation (OLR) data (2006–2016) from Advanced Very High Resolution Radiometer (AVHRR) on board the Kalpana-1 satellite with 0.25° spatial resolution is used to develop the MISO index (Mahakur et al., 2013). MISO events identified during the study period and the events which are used for composites at each mooring location under RAMA-based and OSCAR-based analysis are listed in Table 1. Daily wind data from QuikSCAT (2006–2009) (Wentz et al., 2001) and Advanced Scatterometer (ASCAT) (2009–2016) (Ricciardulli & Wentz, 2016) with 0.25° spatial resolution, OI-SST and daily precipitation from Tropical Rainfall Measuring Mission (TRMM) 3B42 Version 7 (Huffman et al., 2007) are utilized to analyze the spatiotemporal evolution of wind, SST and rainfall variability associated with the MISO, respectively.

We generated a daily climatology by averaging variables each day of the year across all years. We then computed anomalies by subtracting this climatology from the daily time series. Daily data under a particular MISO phase for several events is averaged to generate a MISO composite.

3. Results

RAMA mooring data in the BoB provide an unprecedented opportunity to examine the upper ocean response to MISO over several years. Figure 1, for example, shows time series of near-surface oceanographic and meteorological parameters obtained from RAMA mooring at 15°N, 90°E for the period 2008–2016. Before going to the main topic of this study, here we set the stage by describing some features of the regional climatology in the BoB based on these measurements. Net shortwave radiation reaches its maximum amplitude during spring (~280 W m^{-2}) and minimum during winter (~120 W m^{-2}); moreover, it shows large variability during summer monsoon season when it oscillates between 120 and 250 W m^{-2} due to variations in cloudiness (Figure 1). Net longwave radiation shows strong annual variability with maximum heat loss from the ocean during winter (−90 W m^{-2}) due to clear sky conditions and minimum during summer monsoon season (−20 W m^{-2}) due to extensive cloud cover (Figure 1) (Thangaprakash et al., 2016). Near-surface humidity is relatively high during the summer monsoon (~85%) due to the southwest monsoon winds over the Indian Ocean carrying relatively high humidity air into the BoB from the south; conversely, relative humidity is low during winter (~65%) due to the intrusion of dry continental air into the BoB by the northeast monsoon winds (Figure 1) (Thangaprakash et al., 2016). In general, the near-surface current structure shows high-frequency variability due to eddy activity without any significant seasonal pattern (Figure 1). Near-surface ocean temperature and air temperature from the RAMA mooring indicate two periods of warming during the intermonsoon seasons (March–April and October–November) and two periods of cooling, one during the summer monsoon (May–September) and a second during the winter monsoon (December–February) (Figure 1). The coldest surface temperatures occur during the early part of the calendar year during the winter monsoon season (Rao & Sivakumar, 2000; Shenoi et al., 2002) (Figure 1). Near-surface salinity structure shows persistent occurrence of a halocline in association with the presence of low salinity water (~32 psu) in the near-surface layer (above 30 m) compared to subsurface layer (~34 psu below 30 m) (Figure 1). The BL is relatively thick (60–70 m) during winter in association with a thin mixed layer due to large freshening near the surface, while during spring and summer, the BL and ML are thinner (Figure 1) (Girishkumar et al., 2011; Thadathil et al., 2007). In addition to these seasonal time scale variations, pronounced intraseasonal variations in surface meteorological and upper ocean parameters are evident as well. It is these variations that are the primary focus of our study.

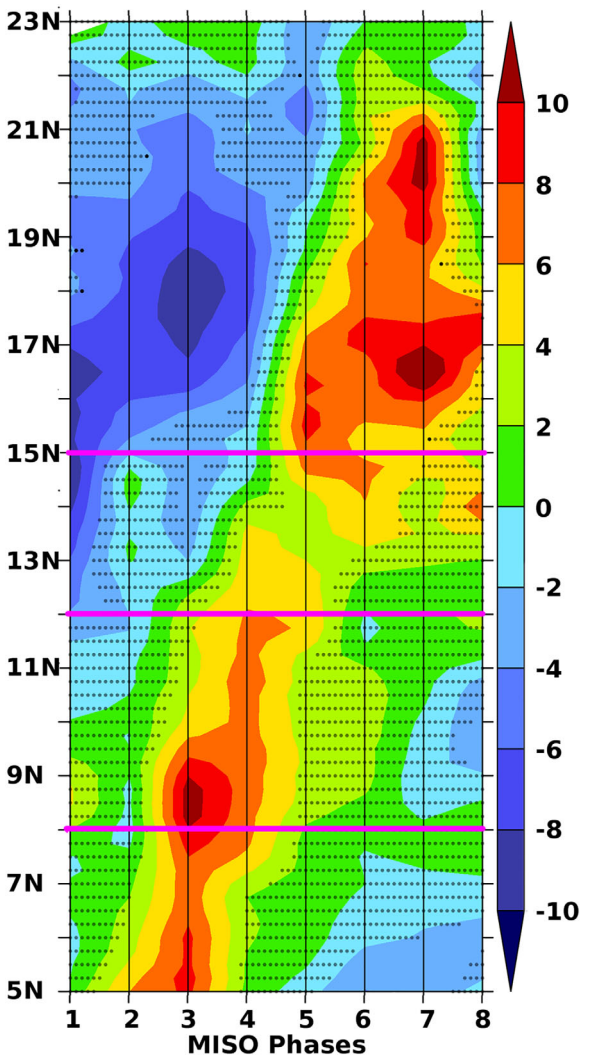

Figure 3. Composite (2007–2016) Hovmöller diagram of TRMM3b42 rainfall anomaly (mm day^{-1}) averaged over 89°E and 91°E in the BoB under different phase of the MISO. Pink horizontal lines indicate RAMA mooring location at 8°N, 12°N, and 15°N, 90°E. Stippling indicates values that are not significantly different from zero at the 90% confidence level using a *t* test.

The composite of spatiotemporal evolution of rainfall anomalies (Figure 2) and Hovmöller diagram of rainfall anomalies (Figure 3) in the central BoB under different phases of the MISO show clear and continuous northward propagation of enhanced and suppressed rainfall activity. Overall, the composite of spatiotemporal variability of rainfall anomalies under different phases of the MISO shows good agreement with well-known evolution of the MISO life cycle as reported in earlier studies (Figure 10 of Suhas et al., 2013). When the MISO is in phase 1, enhanced rainfall activity is prominent over the eastern equatorial Indian Ocean (Figures 2 and 3) and suppressed rainfall activity persistent over the entire BoB. During phases 2–3, enhanced rainfall activity propagates to the southern BoB and suppressed rainfall activity of slightly weaker intensity persists in the northern BoB. During phases 4–6, rainfall activity is enhanced over the entire BoB and core of rainfall maxima propagates progressively northward. During the phases 7–8, MISO rainfall activity is significantly reduced in the entire BoB. In addition, on average the peak rainfall anomaly associated with MISO events at 8°N, 12°N, and 15°N occurs during MISO phases 3, 4, and 5, respectively (Figure 3). For ease

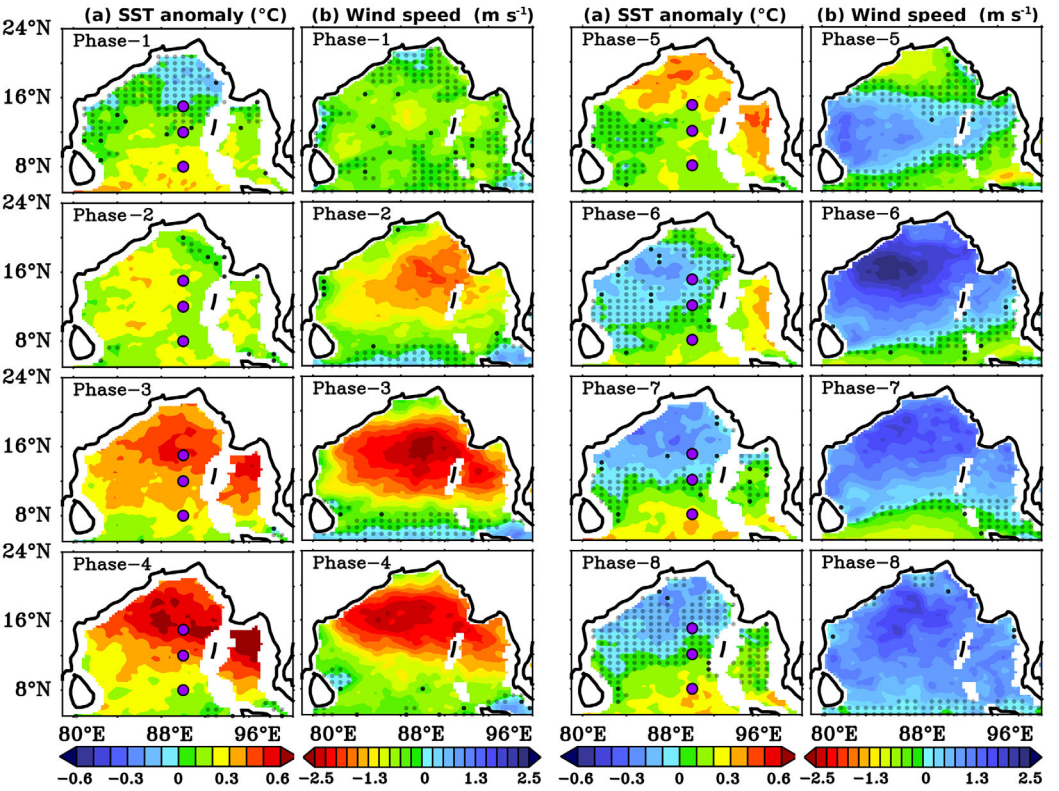

Figure 4. Composite (2007–2016) of (a) OI-SST anomaly (°C) and (b) wind speed anomaly (m s^{-1}; blue for positive anomaly and red for negative anomaly) under different phases of the MISO. The pink circles in the first and third columns indicate RAMA buoy location at 8°N, 12°N, and 15°N, 90°E. Stippling indicates values that are not significantly different from zero at the 90% confidence level using a *t* test.

of discussion in the rest of paper, we define phases 1–2 as the convectively inactive (or suppressed) phase of the MISO and phases 3–6 as the active phase of the MISO with respect to BoB.

With respect to the northward propagation of enhanced and suppressed MISO-related convective activity, the spatiotemporal evolution of composite SST and wind speed anomalies shows distinct spatial structures associated with different MISO phases. Specifically, warm SST anomalies coincide with low wind speeds and vice versa (cf. Figures 2 and 4). In addition, amplitude of MISO-related variability is relatively large in the central and northern BoB (12°N, and 15°N, 90°E) compared to that further south 8°N, 90°E (Figure 4) and the spatial extent of this signal covers approximately half of the basin in the meridional direction. During phase 1, relatively warm SST anomalies of weak intensity (∼0.3°C) persist in the entire BoB except in a small region in the northern BoB. These warm SST anomalies gradually intensify and reach maximum magnitude during MISO phases 3–4. During MISO phase 5, warm SST anomalies diminish and gradually shift to cool anomalies during phases 5–6.

To illustrate the processes controlling MLT under different phase of the MISO, we examine a composite of MLT budget at 8°N, 12°N, and 15°N along 90°E in the BoB (Figure 5). We start with 15°N where the number of MISO events captured by the analysis is relatively large. We compared the results at this location for the RAMA analysis with an analysis where we substituted observed currents with the OSCAR product and the observed fluxes with the Tropflux product (the RAMA+ analysis). The RAMA and RAMA+ analyses show good agreement though there are slight deviations between these two analyses that we attribute to the larger number of samples in the RAMA+ analysis compared to RAMA analysis (Table 1). Nevertheless, the two approaches (RAMA and RAMA+) at 15°N yield similar results (Figure 5; supporting information Figures S4a and S4b) which give us confidence in using the RAMA+ analysis at 8°N and 12°N where fewer MISO events are captured with the pure RAMA analysis. Thus, in the discussion that follows, we will emphasize results from the RAMA+ analysis at 15°N, 12°N, and 8°N.

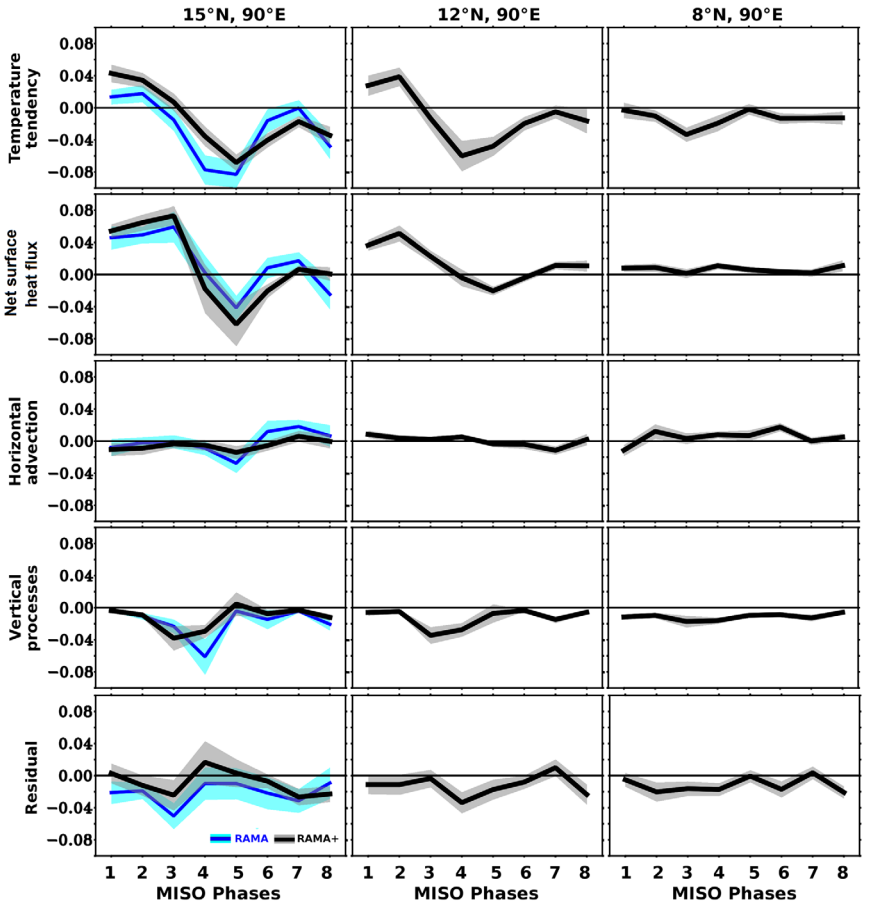

Figure 5. Composite of different terms in the MLT budget equation (temperature tendency, net surface heat flux, horizontal advection, vertical process, and residual) under different MISO phases based on RAMA (blue line) and RAMA+ (black line) analyses at (left plot) 15°N, 90°E, (middle plot) 12°N, 90°E, and (right plot) 8°N, 90°E in the BoB. The blue and gray shading indicates one standard error for RAMA and RAMA+ based analyses. Unit: °C d^{-1}.

Composites of MLT tendency at the mooring locations for different phases of the MISO show similar temporal evolution as observed in SST anomaly tendency (Figure 5 and supporting information Figure S5). In particular, we observe a warming tendency (0.01–0.04°C d^{-1}) during MISO phases 1–2 in conjunction with a strong decreasing tendency in wind speed and convective activity and a cooling tendency (−0.04°C to −0.08°C d^{-1}) with respect to northward movement of enhanced wind speed and convective activity during MISO phases 3–6. We observe a maximum MLT tendency amplitude at the northern BoB site (15°N, 90°E) and a minimum amplitude at the southern site (8°N, 90°E) (Figure 5). Moreover, the MLT cooling tendency reaches its maximum amplitude during MISO phases 3, 4, and 5 at 8°N, 12°N, and 15°N, respectively (Figure 5) consistent with the northward propagating maximum positive rainfall anomaly (Figure 3).

The composite evolution of MLT tendency for different phases of the MISO shows good agreement with sum of net surface heat flux, horizontal advection, and vertical process (Figure 5 and supporting information Figure S4). The main driver of the MLT tendency is the net surface heat flux. Vertical processes also occasionally contribute significantly to the MLT tendency as described a little later in this section. In general, the magnitude of the horizontal advection terms is relatively small (±0.02°C d^{-1}), oscillatory in nature and does not shows any significant trend compared to other terms in the MLT budget equations (Figure 5).

Consistent with amplitude of MLT tendency (Figure 5), net surface heat flux term shows maximum amplitude (−0.07°C d^{-1}) in the northern BoB and minimum (near zero) in the southern BoB (Figure 5), indicating the importance of this term in controlling MISO MLT variations. The RAMA and RAMA+ analyses at 15°N and 12°N show that net surface heat flux ($Q_{net} - Q_{pen}$) is a maximum into the ocean (50 W m^{-2}) during MISO phases 1–2 and maximum out of the ocean (−35 W m^{-2}) during MISO phases 4–5 (Figure 6).

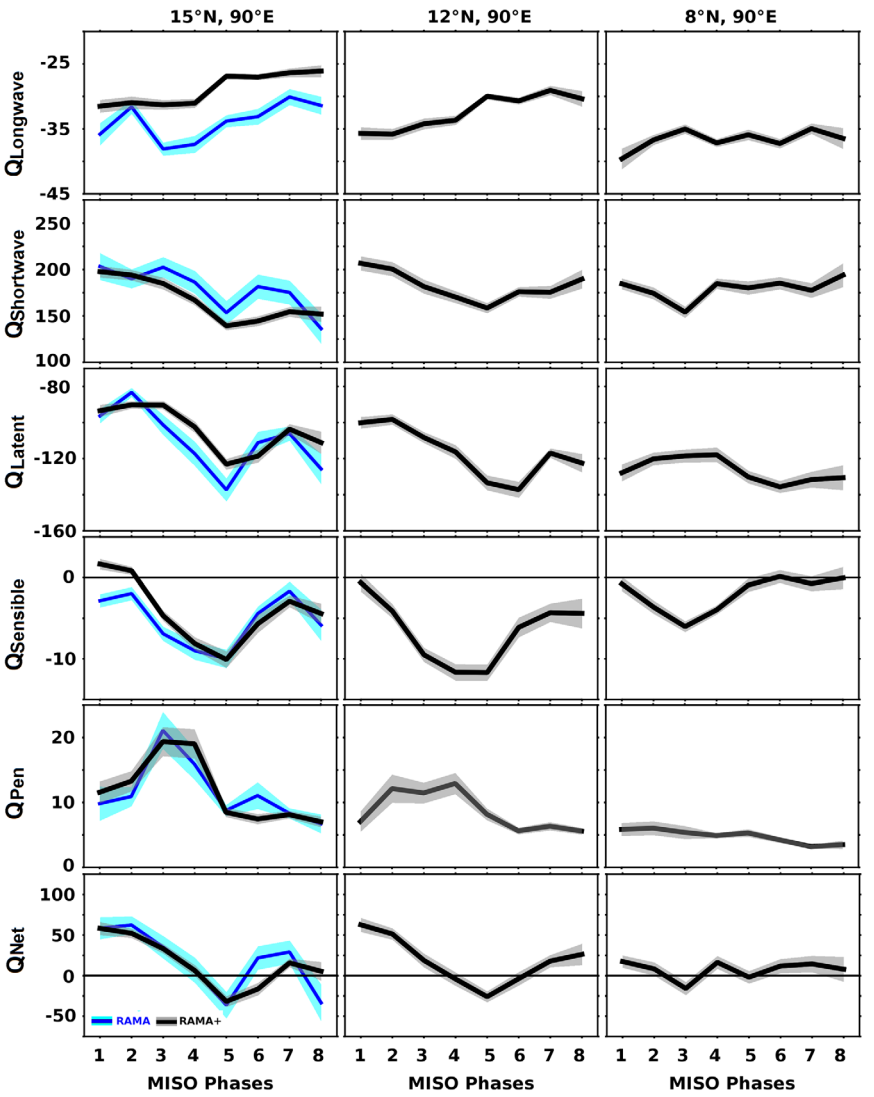

Figure 6. Composite of net longwave radiation ($Q_{Longwave}$), net shortwave radiation ($Q_{Shortwave}$), latent heat flux (Q_{Latent}), sensible heat flux ($Q_{Sensible}$), penetrating shortwave radiation (Q_{Pen}) and net surface heat flux (Q_{Net}) under different MISO phases based on RAMA (blue line) and RAMA+ (black line) analyses at (left plot) 15°N, 90°E, (middle plot) 12°N, 90°E, and (bottom plot) 8°N, 90°E in the BoB. The blue and gray shading indicates one standard error for RAMA and RAMA+ analyses. Unit: W m^{-2}.

However, the variability of net surface heat flux ($Q_{net} - Q_{pen}$) is small at 8°N in comparison with the other mooring locations. The composite evolution of longwave radiation during the MISO event is relatively small and is on average around -35 W m^{-2} (Figure 6). In general, the variability of net surface heat flux ($Q_{net} - Q_{pen}$) is modulated primarily by net shortwave radiation and latent heat flux, of which the former varies between 125 and 200 W m^{-2} while the latter varies between -80 and -150 W m^{-2} from inactive to active phases of the MISO (Figure 6). At 15°N and 12°N, Q_{pen} shows maximum heat loss ($\sim$20 W m^{-2}) below the mixed layer during phases 3–4 which coincide with the periods of shallowest MLD ($\sim$25 m) (Figures 6 and 7). Otherwise this term is relatively small ($<$10 W m^{-2}) in conjunction with MLDs of $\sim$40–50 m (Figures 6 and 7). The role of Q_{pen} is relatively weak at 8°N, due to the relatively deep mixed layer ($>$40 m) throughout the MISO life cycle at this location (Figures 6 and 7).

Sensible heat flux is small, being near zero during the inactive phase with increasing heat loss (-10 W m^{-2}) from the ocean during the active phase of the MISO (Figure 6). The average increase in wind speed from the inactive phase to the active phase of MISO is relatively small ($\sim$2 m s^{-1}) (Figure 8) so most of the variations in sensible heat flux are due to air-sea temperature differences. The temperature between the ocean

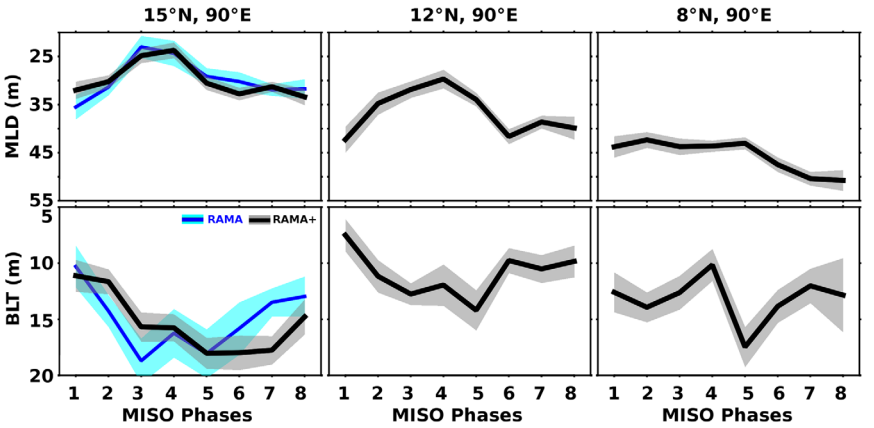

Figure 7. Composite of MLD (m) and BLT (m) under different MISO phases based on RAMA (blue line) and RAMA+ (black line) analysis at (left plot) 15°N, 90°E, (middle plot) 12°N, 90°E, and (right plot) 8°N, 90°E in the BoB. The blue and gray shading indicates one standard error for RAMA and RAMA+ analyses.

and air differs by a factor of 3 during the convectively active phase (SST-AIRT $\sim$ 1°C) compared to the convectively inactive (SST-AIRT $\sim$ 0.3°C) phase of the MISO (Figure 8). Similarly, the difference in specific humidity (q_s–q_a) between ocean surface (q_s) and air (q_a) varies from 3.4 g kg^{-1} during the inactive phase of MISO to 4.2 g kg^{-1} during active phase of MISO (Figure 8). These features are more prominent at the 12°N and 15°N mooring locations than at 8°N. The strong temporal correspondence between turbulent heat flux and air-sea temperature and humidity differences though indicates that variations in these properties are primarily responsible for the enhancement of sensible and latent heat loss during the active phases of the MISO.

It is worth noting here that there is a significant difference in the evolution of SST and q_s vis a vis air temperature and q_a during MISO events (Figure 8). Though both SST and q_s show an increasing tendency up to phase 4 at 12°N and 15°N, air temperature and q_a lead SST and q_s by two MISO phases. The reduction in near-surface air temperature and q_a is likely to be associated with downdrafts from northward propagating convective systems. In the downdraft region of MISO convective systems, rain-filled air can mix with unsaturated environmental air leading to evaporative cooling due to absorption of latent heat. Downdrafts bring dry and cold upper air to the surface boundary layer and this air spreads out to replace relatively warm and humid air, leading to a reduction in near-surface air temperature and q_a. In addition, the background mean southwesterly wind (Figure 1 and supporting information Figure S6) can spread this downdraft air northward much faster than northward propagating convective anomaly, which may explain why reduced air temperature and q_a lead SST and q_s. As further support for this argument, we point out that the composite maps of rainfall and rainfall anomaly show that maximum rainfall reaches 12°N and 15°N around phases 4 and 5, respectively (Figure 3). However, the reduction in air temperature starts by phases 1 and 2 at 12°N and 15°N (Figure 8). Similar tendencies are also observed at 8°N.

Though the net surface heat flux plays an important role, it cannot completely explain the observed evolution of MLT tendency during MISO events. Our analysis shows that vertical processes can also play an important role, particularly during periods of MLT cooling with a maximum contribution of -0.02 to -0.06°C d^{-1} during phases 3–4 (Figure 5). Moreover, consistent with the MLT tendency (Figure 5) and net surface heat flux (Figure 5), the contribution of vertical processes on the MLT budget increases toward the north (Figure 5). Specifically, the cooling due to vertical processes is relatively large at 15°N (-0.06°C d^{-1}) and relatively weak at 8°N (-0.01°C d^{-1}). Moreover, the mean BLT is only 10–15 m during entire MISO life cycle (Figure 7), which allows for relatively free turbulent transport of cold thermocline water into ML (see supporting information Text S2 and Figure S7) for how turbulent vertical transport can occur in the presence of relatively thin barrier layers). Thus, entrainment cooling makes a substantial contribution to the MLT cooling tendency during phases 3–4 at 12°N, 90°E and 15°N, 90°E since net surface heat flux is weakly positive at this time (Figure 5; supporting information Figures S4a, S4b, and S4c). To a certain extent a similar tendency can also be seen at 8°N, 90°E, where vertical process shows a mild cooling tendency during phases 2–4 when MLT shows cooling tendency (Figure 5 and supporting information Figure S4d). In

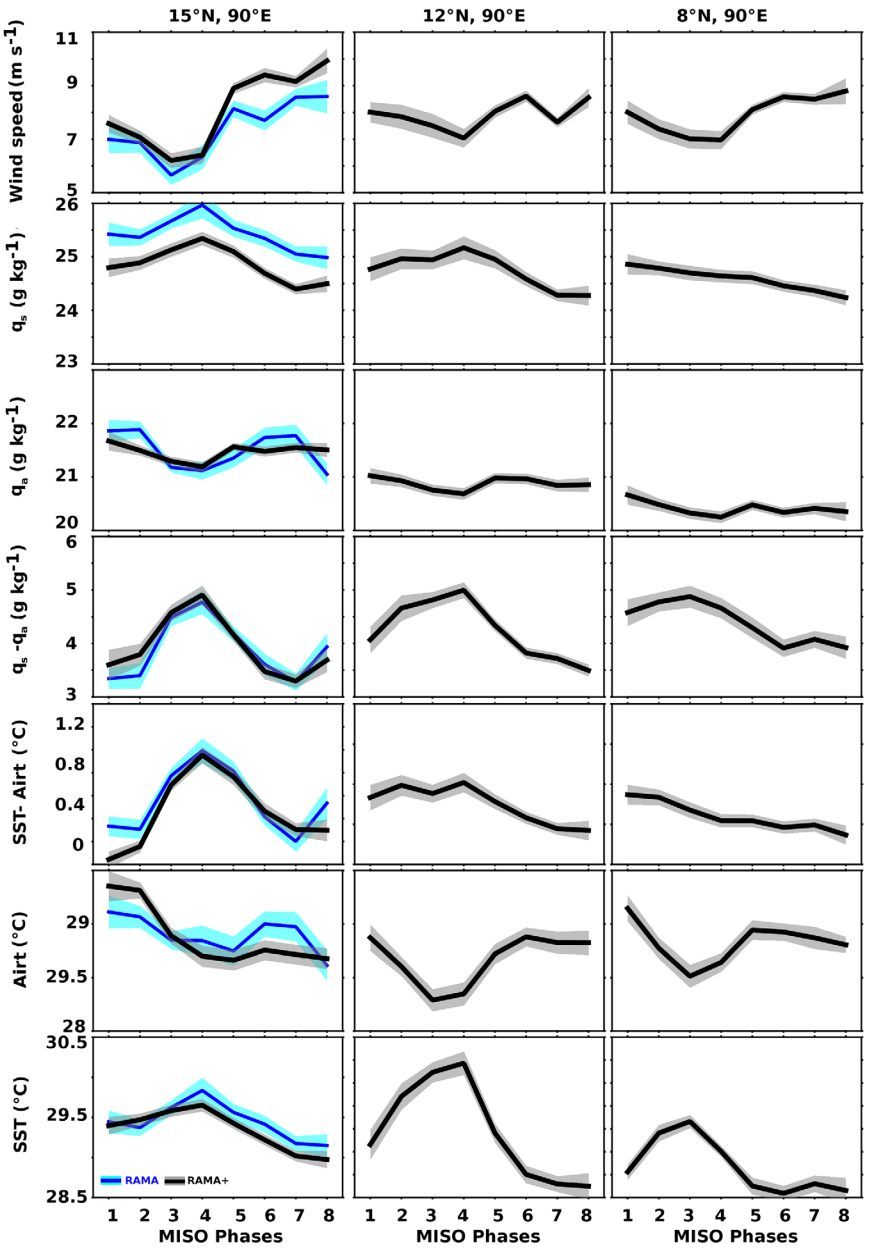

Figure 8. Composite of wind speed (m s^{-1}), specific humidity of sea surface (q_s; g kg^{-1}), specific humidity of air (q_a; g kg^{-1}), specific humidity difference between sea surface and air (q_s; g kg^{-1}), difference between SST and air temperature (°C), air temperature (°C), and SST (°C) under different MISO phases based on RAMA (blue line) and RAMA+ (black line) analyses at (left plot) 15°N, 90°E, (middle plot) 12°N, 90°E, and (right plot) 8°N, 90°E in the BoB. The blue and gray shading indicates one standard error for RAMA and RAMA+ analyses.

summary, net surface heat flux, complemented by entrainment cooling during phases 3–4, are the main determinants of the observed evolution of MLT during the MISO events.

4. Summary and Conclusion

In this study, we used upper oceanographic and surface meteorological observations from RAMA buoys at 8°N, 12°N, and 15°N along 90°E together with meteorological parameters from the TropFlux product and ocean currents from the OSCAR velocity product to analyze near-surface variability in the BoB associated with the response to northward propagating MISO convective anomalies. Composite averages of MLT

budget terms and near-surface meteorological and oceanographic parameters over various MISO events are used to evaluate the air-sea interaction processes and oceanic processes responsible for MLT variations at MISO time scales in the central BoB.

We find that a strong MLT warming tendency is linked to the northward propagation of suppressed convection associated with MISO events and a strong MLT cooling tendency is linked to the northward propagation of active MISO convection. At the mooring locations, the MLT warming tendency during inactive phases of the MISO is primarily due to net surface heat flux into the ocean. During MISO active phases on the other hand, MLT strongly cools in response to a near zero or net heat loss from the ocean to the atmosphere plus entrainment cooling at the base of ML. The variability of net surface heat flux is primarily due to the modulation of latent heat flux and shortwave radiation, in which the latter is controlled by enhancement or reduction of cloudiness during the active and inactive phases of the MISO, respectively. Our analysis further indicates that enhancement of latent heat loss during the active phase of the MISO is primarily due to air-sea humidity differences, which varies from 3.4 g kg^{-1} during the inactive MISO phase to 4.2 g kg^{-1} during active MISO phase. The difference in temperature between ocean and air also varied by a factor of 3 during the convectively active phase (SST-AIRT $\sim$ 1°C) compared to suppressed phase (SST-AIRT $\sim$ 0.3°C) of the MISO. This change leads to an increase in sensible heat loss from the ocean (-10 W m^{-2}) during active phase of MISO compared to near zero value during the inactive phase. These variations in radiative and turbulent heat flux lead to an approximately 60 W m^{-2} net surface heat flux into the ocean during inactive phases of the MISO compared to approximately 35 W m^{-2} net surface heat loss from the ocean during active phases of the MISO. Moreover, the present study highlights that entrainment cooling can play an important role on MLT balance during active phases of the MISO as well.

It is worth pointing out that there is variation in the northward translation speed, amplitude, and spatial structure of individual MISO events. Hence, our composite procedure produces a smoothed depiction of MISO variability. Nevertheless, the present analysis provides new insights on how air-sea interaction affects the evolution of the MISO and how MISO variability affects intraseasonal MLT fluctuations in the BoB. Our analysis also emphasizes the importance representing the upper oceanic and air-sea interaction processes that modulate SST variations associated with MISO accurately in coupled models used for seasonal and subseasonal monsoon forecasting.

The fresh water flux into the BoB from continental rivers begins to increase from May, reaching its peak in August during the summer monsoon (Pant et al., 2015; Rao & Sivakumar, 2003). Hence, the role of near-surface saline stratification may not be uniform throughout the summer monsoon season in the BoB, which could affect late season versus early season MISO events. This issue may require further research. Also, in our study we used monthly average of chlorophyll to estimate penetrative shortwave radiation. However, the presence of significant cloud cover during the summer monsoon in the BoB obscures satellite based chlorophyll measurements. Past studies have reported the enhancement of chlorophyll in the BoB in response to northward propagating convectively anomaly (Jin et al., 2012). Hence, the response of the chlorophyll distribution to MISO events and its impact on the MLT budget through modulation of penetrative shortwave radiation are worthy of investigation. The availability of chlorophyll and subsurface radiometer observations on moorings and from Autonomous Underwater Vehicles such as gliders and biogeochemical Argo floats would facilitate this kind of analysis. Finally, variations in the amplitude and duration of individual MISO events and their impact on MLT are a topic for future study.

Acknowledgments
The encouragement provided by the Director, INCOIS is gratefully acknowledged. QuikSCAT and ASCAT data were produced by Remote Sensing Systems (www.ssmi.com) and are funded by the NASA Ocean Vector Winds Science Team. Graphics are generated using PyFerret. RAMA data are available from PMEL (https://www.pmel.noaa.gov/gtmba/pmel-theme/indian-ocean-rama). TropFlux products are available from http://www.incois.gov.in/tropflux and the OSCAR current product is available from http://www.esr.org/oscar_index.html. TRMM3b42 precipitation product is available from http://iridl.ldeo.columbia.edu. We thank two anonymous reviewers for their valuable suggestions on an earlier version of this manuscript. This is INCOIS contribution 308 and PMEL contribution 4660.

References

Annamalai, H., & Slingo, J. M. (2001). Active/break cycles: Diagnosis of the intraseasonal variability of the Asian summer monsoon. *Climate Dynamics*, *18*, 85–102. https://doi.org/10.1007/s003820100161

Bhat, G. S., Vecchi, G. A., & Gadgil, S. (2004). Sea surface temperature of the Bay of Bengal derived from the TRMM microwave imager. *Journal of Atmospheric and Oceanic Technology*, *21*, 1283–1290. https://doi.org/10.1175/1520-0426(2004)021<1283:SSTOTB>2.0.CO;2

Bonjean, F., & Lagerloef, G. S. E. (2002). Diagnostic model and analysis of the surface currents in the tropical Pacific Ocean. *Journal of Physical Oceanography 32*, 2938–2954. https://doi.org/10.1175/1520-0485(2002)032<2938:DMAAOT>2.0.CO;2

Chi, N.-H., Lien, R.-C., D'asaro, E. A., & Ma, B. B. (2014). The surface mixed layer heat budget from mooring observations in the central Indian Ocean during Madden-Julian Oscillation events. *Journal of Geophysical Research: Oceans*, *119*, 4638–4652. https://doi.org/10.1002/2014JC010192

Drushka, K., Sprintall, J., Gille, S. T., & Wijffels, S. (2012). In situ observations of Madden-Julian Oscillation mixed layer dynamics in the Indian and western Pacific Oceans. *Journal of Climate*, *25*, 2306–2328. https://doi.org/10.1175/JCLI-D-11-00203.1

Du, Y., Qu, T., Meyers, G., Masumoto, Y., & Sasaki, H. (2005). Seasonal heat budget in the mixed layer of the southeastern tropical Indian Ocean in a high-resolution ocean general circulation model. *Journal of Geophysical Research*, *110*, C04012. https://doi.org/10.1029/2004JC002845

Fairall, C. W., Bradley, E. F., Hare, J. E., Grachev, A. A., & Edson, J. B. (2003). Bulk parameterization of air-sea fluxes: Updates and verification for the COARE algorithm. *Journal of Climate*, *16*, 571–591. https://doi.org/10.1175/1520-0442(2003)016<0571:BPOASF>2.0.CO;2

Foltz, G. R., & McPhaden, M. J. (2009). Impact of barrier layer thickness on SST in the central tropical North Atlantic. *Journal of Climate*, *22*, 285–299. https://doi.org/10.1175/2008JCLI2308.1

Fu, X., & Wang, B. (2004). The boreal-summer intraseasonal oscillations simulated in a hybrid coupled atmosphere-ocean model. *Monthly Weather Review*, *132*, 2628–2649. https://doi.org/10.1175/MWR2811.1

Girishkumar, M. S., Ravichandran, M., & McPhaden, M. J. (2013). Temperature inversions and their influence on the mixed layer heat budget during the winters of 2006–2007 and 2007–2008 in the Bay of Bengal. *Journal of Geophysical Research: Oceans*, *118*, 2426–2437. https://doi.org/10.1002/jgrc.20192

Girishkumar, M. S., Ravichandran, M., McPhaden, M. J., & Rao, R. R. (2011). Intraseasonal variability in barrier layer thickness in the south central Bay of Bengal. *Journal of Geophysical Research*, *116*, C03009. https://doi.org/10.1029/2010JC006657

Gentemann, C. L., Wick, G. A., Cummings, J., & Bayler, E. (2004). Multi-sensor improved sea surface temperature (MISST) for GODAE Paper presented at 13th Conference on Satellite Meteorology and Oceanography, Norfolk, VA, USA, 19–23 September, 2004. Retrieved from http://www.remss.com/papers/gentemann/gentemann_13satmet_2004.pdf

Goswami, B. N. (2011). South Asian summer monsoon. In W. K.-M. Lau & D. E. Waliser (Eds.), *Intraseasonal variability of the atmosphere-Ocean climate system* (2nd ed., pp. 21–72). Berlin, Germany: Springer.

Goswami, B. N., & Ajaya Mohan, R. S. (2001). Intraseasonal oscillations and interannual variability of the Indian summer monsoon. *Journal of Climate*, *14*(6), 1180–1198. https://doi.org/10.1175/1520-0442(2001)014<1180:IOAIVO>2.0.CO;2

Goswami, B. N., Rao, S. A., Sengupta, D., & Chakravorty, S. (2016). Monsoons to mixing in the Bay of Bengal: Multiscale air-sea interactions and monsoon predictability. *Oceanography*, *29*(2), 18–27. https://doi.org/10.5670/oceanog.2016.35

Goswami, B. N., Wu, G., & Yasunari, T. (2006). Annual cycle, intraseasonal oscillations and roadblock to seasonal predictability of the Asian summer monsoon. *Journal of Climate*, *19*, 5078–5099. https://doi.org/10.1175/JCLI3901.1

Huffman, G. J., Adler, R. F., Bolvin, D. T., Gu, G., Nelkin, E. J., Bowman, K. P., . . . Wolff, D. B. (2007). The TRMM multi-satellite precipitation analysis: Quasi-global, multi-year, combined-sensor precipitation estimates at fine scale. *Journal of Hydrometeorology*, *8*(1), 38–55.

Jin, D., Murtugudde, R., & Waliser, D. E. (2012). Tropical Indo-Pacific Ocean chlorophyll response to MJO forcing. *Journal of Geophysical Research*, *117*, C11008. https://doi.org/10.1029/2012JC008015

Lin, J., Kiladis, G., Mapes, B., Weickmann, K., Sperber, K., Lin, W., . . . Scinocca, J. (2006). Tropical intraseasonal variability in 14 IPCC AR4 climate models. Part I: Convective signals. *Journal of Climate*, *19*, 2665–2690. https://doi.org/10.1175/JCLI3735.1

Kemball-Cook, S., Wang, B. & Fu, X. (2002). Simulation of the intraseasonal oscillation in the ECHAM-4 model: The impact of coupling with an ocean model. *Journal of the Atmospheric Sciences*, *59*, 1433–1453. https://doi.org/10.1175/1520-0469(2002)059<1433:SOTIOI>2.0.CO;2

Madden, R. A., & Julian, P. R. (1994). Observations of the 40–50-day tropical oscillation: A review. *Monthly Weather Review*, *122*, 814–837. https://doi.org/10.1175/1520-0493(1994)122<0814:OOTDTO>2.0.CO;2

Mahakur, M., Prabhu, A., Sharma, A., Rao, V., Senroy, S., Singh, R., & Goswami, B. (2013). A high-resolution outgoing longwave radiation dataset from Kalpana-1 satellite during 2004–2012. *Current Science*, *105*(8), 1124–1133. Retrieved from http://www.jstor.org/stable/24098219

McPhaden, M. J. (1982). Variability in the central equatorial Indian Ocean, Part II: Oceanic heat and turbulent energy balance. *Journal of Marine Research*, *40*, 403–419.

McPhaden, M. J., & Foltz, G. R. (2013). Intraseasonal variations in the surface layer heat balance of the central equatorial Indian Ocean: The importance of zonal advection and vertical mixing. *Geophysical Research Letters*, *40*, 2737–2741. https://doi.org/10.1002/grl.50536

McPhaden, M. J., Meyers, G., Ando, K., Masumoto, Y., Murty, V. S. N., Ravichandran, M., . . . Yu, W. (2009). RAMA: The research moored array for African-Asian-Australian Monsoon analysis and prediction. *Bulletin of the American Meteorological Society*, *90*, 459–480. https://doi.org/10.1175/2008BAMS2608.1

Morel, A., & Antoine, D. (1994). Heating rate within the upper ocean in relation to its bio-optical state. *Journal of Physical Oceanography*, *24*, 1652–1665. https://doi.org/10.1175/1520-0485(1994)024<1652:HRWTUO>2.0.CO;2

Pant, V., Girishkumar, M. S., Udaya Bhaskar, T. V. S., Ravichandran, M., Papa, F., & Thangaprakash, V. P. (2015). Observed interannual variability of near-surface salinity in the Bay of Bengal. *Journal of Geophysical Research: Oceans*, *120*, 3315–3329. https://doi.org/10.1002/2014JC010340

Parampil, S. R., Gera, A., Ravichandran, M., & Sengupta, D. (2010). Intraseasonal response of mixed layer temperature and salinity in the Bay of Bengal to heat and freshwater flux. *Journal of Geophysical Research*, *115*, C05002. https://doi.org/10.1029/2009JC005790

Praveen Kumar, B., Vialard, J., Lengaigne, M., Murty, V. S. N., & McPhaden, M. J. (2012). TropFlux: Air-sea fluxes for the global tropical oceans—Description and evaluation. *Climate Dynamics*, *38*, 1521–1543. https://doi.org/10.1007/s00382-011-1115-0

Rao, R. R., & Sivakumar, R. (2000). Seasonal variability of near-surface thermal structure and heat budget of the mixed layer of the tropical Indian Ocean from a new global ocean temperature climatology. *Journal of Geophysical Research*, *105*(C1), 995–1015. https://doi.org/10.1029/1999JC900220

Rao, R. R., & Sivakumar, R. (2003). Seasonal variability of sea surface salinity and salt budget of the mixed layer of the north Indian Ocean. *Journal of Geophysical Research*, *108*(C1), 3009. https://doi.org/10.1029/2001JC000907

Ricciardulli, L., & Wentz, F. J. (2016). *Remote Sensing Systems ASCAT C-2015 Daily Ocean Vector Winds on 0.25 deg grid* (Version 2.1). Santa Rosa, CA: Remote Sensing Systems. Retrieved from www.remss.com/missions/ascat

Roxy, M., Tanimoto, Y., Preethi, B., Pascal, T., & Krishnan, R. (2012). Intraseasonal SST-precipitation relationship and its spatial variability over the tropical summer monsoon region. *Climate Dynamics*, *41*, 45–61. https://doi.org/10.1007/s00382-012-1547-1

Sengupta, D., Goswami, B. N., & Senan, R. (2001). Coherent intraseasonal oscillations of the ocean and atmosphere during the Asian summer monsoon. *Geophysical Research Letters*, *28*(21), 4127–4130.

Seo, K. H., Schemm, J. K. E., Wang, W., & Kumar, A. (2007). The boreal summer intraseasonal oscillation simulated in the NCEP Climate Forecast System: The effect of sea surface temperature. *Monthly Weather Review*, *135*, 1807–1827. https://doi.org/10.1175/MWR3369.1

Sharmila, S., Pillai, P. A., Joseph, S., Roxy, M., Krishna, R. P. M., Chattopadhyay, R., . . . Goswami, B. N. (2013). Role of ocean-atmosphere interaction on northward propagation of Indian summer monsoon intraseasonal oscillations. *Climate Dynamics*, *41*, 1651–1669. https://doi.org/10.1007/s00382-013-1854-1

Shenoi, S. S. C., Shankar, D., & Shetye, S. R. (2002). Differences in heat budgets of the near-surface Arabian Sea and Bay of Bengal: Implications for the summer monsoon. *Journal of Geophysical Research*, *107*(C6), 3052. https://doi.org/10.1029/2000JC000679

Sikhakolli, R., Sharma, Basu, R. S., Gohil, B., Sarkar, S. A., & Prasad, K. V. S. R. (2012). Evaluation of OSCAR ocean surface current product in the tropical Indian Ocean using in situ data. *Journal of Earth System Science*, *122*(1), 187–199.

Sikka, D. R., & Gadgil, S. (1980). On the maximum cloud zone and the ITCZ over Indian, longitudes during the southwest monsoon. *Monthly Weather Review*, *108*, 1840–1853. https://doi.org/10.1175/1520-0493(1980)108<1840:OTMCZA>2.0.CO;2

Sivareddy, S., Ravichandran, M., Girishkumar, M. S., & Prasad, K. V. S. R. (2015). Assessing the impact of various wind forcing on INCOIS-GODAS simulated ocean currents in the equatorial Indian Ocean. *Ocean Dynamics*, *65*, 1235–1247. https://doi.org/10.1007/s10236-015-0870-6

Suhas, E., Neena, J. M., & Goswami, B. N. (2013). An Indian monsoon intra-seasonal oscillations (MISO) index for real time monitoring and forecast verification. *Climate Dynamics*, *40*, 2605–2616. https://doi.org/10.1007/s00382-012-1462-5

Thadathil, P., Muraleedharan, P. M., Rao, R. R., Somayajulu, Y. K., Reddy, G. V., & Revichandran, C. (2007). Observed seasonal variability of barrier layer in the Bay of Bengal. *Journal of Geophysical Research*, *112*, C02009. https://doi.org/10.1029/2006JC003651

Thangaprakash, V. P., Girishkumar, M. S., Suprit, K., Kumar, N. S., Chaudhuri, D., Dinesh, K., . . . & Weller, R. A. (2016). What controls seasonal evolution of sea surface temperature in the Bay of Bengal? Mixed layer heat budget analysis using moored buoy observations along 90°E. *Oceanography*, *29*(2), 202–213. https://doi.org/10.5670/oceanog.2016.52

Varkey M. J., Murty, V. S. N., & Suryanarayana, A. (1996). Physical oceanography of the Bay of Bengal and Andaman Sea. In A. D. Ansell, R. N. Gibson, & M. Barnes (Eds.), *Oceanography and marine biology: An annual review* (vol. 34, pp. 1–70). London: Allen and Unwin.

Vecchi, G. A., & Harrison, D. E. (2002). Monsoon breaks and sub seasonal sea surface temperature variability in the Bay of Bengal. *Journal of Climate*, *15*, 1485–1493. https://doi.org/10.1175/1520-0442(2002)015<1485:MBASSS>2.0.CO;2

Vialard, J., Foltz, G. R., McPhaden, M. J., Duvel, J. P., & de Boyer Montégut, C. (2008). Strong Indian Ocean sea surface temperature signals associated with the Madden-Julian Oscillation in late 2007 and early 2008. *Geophysical Research Letters*, *35*, L19608. https://doi.org/10.1029/2008GL035238

Wang, B., Webster, P., Kikuchi, K., Yasunari, T., & Qi, Y. J. (2006). Boreal summer quasi-monthly oscillation in the global tropics. *Climate Dynamics*, *27*, 661–675.

Webster, P., Bradley, E., Fairall, C., Godfrey, J., Hacker, P., Houze, R., . . . & Zuidema, P. (2002). The JASMINE Pilot Study. *Bulletin of the American Meteorological Society*, *83*, 1603–1630. https://doi.org/10.1175/BAMS-83-11-1603

Wentz, F. J., Smith, D. K., Mears, C. A., & Gentemann, C. L. (2001). Advanced algorithms for QuikSCAT and SeaWinds/AMSR. In *IEEE 2001 international geoscience and remote sensing symposium* (vol. 3, pp. 1079–1081). New York: Inst. of Electr. and Electr. Eng. https://doi.org/10.1109/IGARSS.2001.976752

Wheeler, M. C., & Hendon, H. H. (2004). An all-season real-time multivariate MJO index: Development of an index for monitoring and prediction. *Monthly Weather Review*, *132*(8), 1917–1932.

Yasunari, T. (1979). Cloudiness fluctuation associated with the northern hemisphere summer monsoon. *Journal of Meteorological Society of Japan*, *57*, 227–242. https://doi.org/10.2151/jmsj1965.57.3_227